RSC Advances

PAPER

View Article Online
View Journal | View Issue

Cite this: *RSC Adv.*, 2026, **16**, 25758

Cost-effective preparation of cobalt oxide/nickel oxide composite for the efficient non-enzymatic electrochemical detection of uric acid

Arslan Uddin Qureshi,[a] Humaira Khan,[a] Aneela Tahira,[b] Shaista Bano Memon,[i] Asma Hayat,[aj] Saba Naz,[a] Muhammad Ali Bhatti,[d] Aftab Ahmed Khand,[c] Matteo Tonezzer,[e] Brigitte Vigolo,[f] Elmuez Dawi,[g] Rafat M. Ibrahim[h] and Zafar Hussain Ibupoto *[a]

This study underscores the potential of *Cucumis melo* juice as a sustainable reducing, structure-directing, capping, and stabilizing agent used to modify the surface characteristics, shape, and size of nickel oxide (NiO) through a modified hydrothermal process. This modification results in a significant alteration of the optical band gap of NiO, which is subsequently utilized in combination with cobalt oxide (Co_3O_4) to synthesize Co_3O_4/NiO composites. The physical and optical properties of the synthesized materials, including their morphology, crystal structure, and optical behavior, were thoroughly examined using advanced analytical techniques, such as scanning electron microscopy (SEM), powder X-ray diffraction (XRD), and UV-visible spectrometry, while the chemical bonds within these materials were investigated through Fourier transform infrared (FTIR) spectroscopy. Among the composites, the reduced Co_3O_4/NiO-1 composite, characterized by an optical bandgap of 2.07 eV, exhibited the most pronounced activity for electrochemical non-enzymatic detection of uric acid (UA). This particular composite demonstrated a broad operational range, capable of detecting UA at concentrations from 0.1 mM to 16 mM using the chronoamperometric method. Additionally, it achieved a high sensitivity of 7.63×10^{-4} μA mM^{-1} cm^{-2} and a low detection limit of 0.005 mM when tested in a 0.1 M phosphate buffer solution at a pH of 7.3.

Received 23rd February 2026
Accepted 25th April 2026

DOI: 10.1039/d6ra01598k

rsc.li/rsc-advances

1 Introduction

During purine metabolism, uric acid (UA) is produced as a final product due to the lack of the uricase enzyme in the human body.[1] Generally, serum UA levels in men range from 200 to 430 micromoles per litre (μM) (3.4 to 7.2 milligrams per decilitre (mg dL^{-1})) and in women from 140 to 360 μM (2.4 to 6.1 mg dL^{-1}).[2] If UA levels exceed these ranges, abnormalities can cause a variety of health problems, including the Lesch-Nyhan syndrome, high blood pressure, gout, and kidney disease.[3] The presence of a high UA level, greater than 7.0 mg dL^{-1} in men and 6.0 mg dL^{-1} in women, results in the acidification of body fluids, affecting cell function and increasing the risk of kidney failure and leukemia.[4] This makes the accurate measurement of UA essential for monitoring and diagnosing diseases.[5] A number of methods have been developed for the determination of UA, including chromatography, chemiluminescence, colorimetry, capillary electrophoresis, spectrophotometry, mass spectrometry, as well as non-enzymatic electrochemical sensors and enzymatic biosensors.[6–10] Several of these analytical methods involve complicated procedures that require a significant amount of time and money.[11] An enzymatic approach is typically used in most electrochemical UA sensors because of their high sensitivity, simple operation, speed, ease of operation, and excellent selectivity.[12,13] Due to the high cost of enzymes and storage issues caused by environmental factors, enzymatic biosensors are not of high consideration for large-scale production. Moreover, enzymatic electrochemical biosensors utilize complicated enzyme immobilization techniques, and the high sensitivity of enzymes cannot be ignored. Recent research has focused on the development of enzyme-free sensors, where largely nanostructured

[a]*Institute of Chemistry, University of Sindh, Jamshoro 76080, Pakistan. E-mail: zaffar.ibhupoto@usindh.edu.pk*
[b]*Institute of Chemistry, Shah Abdul Latif University Khairpur Mirs, Sindh, Pakistan*
[c]*Department of Physiology and MLT, University of Sindh, Jamshoro, Pakistan*
[d]*Centre for Environmental Sciences, University of Sindh Jamshoro, Sindh, 76080, Pakistan*
[e]*Department of Chemical and Geological Sciences, University of Cagliari, Monserrato, Italy*
[f]*Université de Lorraine, CNRS, Institut Jean Lamour-IJL, F-54000 Nancy, France*
[g]*College of Humanities and Sciences, Department of Mathematics and Sciences, Ajman University, P.O. Box 346, Ajman, United Arab Emirates*
[h]*Physics Department, College of Science, Taibah University, Madainah, Saudi Arabia*
[i]*Institute of Microbiology, University of Sindh, Jamshoro (76080), Pakistan*
[j]*Department of Chemistry, Turbat University, Turbat Balchistant, Pakistan*

materials have been used to overcome these challenges. These sensors are simple, exhibit excellent sensitivity, and are cost-effective.[14] Due to their inherent affordability, portability, and ease of handling, metal oxide nanostructure-based sensors are emerging as a highly viable platform for point-of-care health monitoring.[15] Transition metal oxides possess excellent redox properties, including high electrical conductivity and abundant catalytic sites, enabling their use in next-generation electrochemical biomedical devices.[16,17] The development of electrochemical biosensors has been achieved by modifying metal oxide nanostructures with conducting polymers.[18,19] Incorporating a variety of functional groups creates favourable electrochemical mediation between polymers and nanomaterials, thus facilitating the efficient transfer of electrons during the detection of biomolecules.[20,21] Cobalt oxide (Co_3O_4) is a p-type semiconductor that provides an excess hole strength and helps to capture electrons during UA oxidation.[22] There have been several methods used to prepare Co_3O_4 shapes, including chemical vapor deposition, sol–gel, wet chemical, and electrophoretic methods.[23] Due to their rapid electron transport and excellent electrocatalytic properties, these diverse morphologies of Co_3O_4 have been utilized in electrochemical detection, energy storage, and conversion technologies.[24–28] The Co_3O_4 nanostructures have been chosen as the preferred surface modification of electrodes due to their improved electrochemical performance and electrical conductivity for the fabrication of non-enzymatic sensors.[29,30] A composite system of Co_3O_4 has been associated with tunable metal oxidation states, tailored morphology, enhanced electron transport, and enriched redox chemistry.[31] However, many of these Co_3O_4-based composites have been prepared through complicated and costly methods; thus, new strategies for the facile and low-cost preparation of Co_3O_4 composite materials need to be developed.

This is the reason a large number of metal oxide composites have been prepared and demonstrated for a wide range of applications, such as supercapacitors,[32] sensors,[33] solar cells,[34] and photocatalysis,[35] and bacterial applications.[36] Having improved active surface area, large surface area, high electron transfer rate, and minimum electron–hole recombination, these composites have demonstrated excellent performance in real-time applications.[37] In comparison with their separate production, the merging of Co_3O_4 and nickel oxide (NiO) creates a synergetic effect in terms of modifying electrical conductance, surface area, catalytic sites, and stability.[38] NiO is a semiconducting, electrochemically stable, catalytically active and earth-abundant material.[39] There is, however, a limitation to the widespread use of NiO due to its wide optical bandgap, and Co_3O_4 possesses a narrow bandgap, spinel structure, and enhanced catalytic sites.[40,41] As a result, the combination of NiO and Co_3O_4 can result in unique structures and functionalities with tailor-made electrochemical properties. These aspects of the development of NiO and Co_3O_4 composites point to the growing interest in investing in these materials for a wide range of applications. The synthetic methods have an important impact on the properties of the material, such as its surface properties, catalytic sites, particle size, charge transfer at the interface, and electrochemical activity. A green synthesis of metal oxide nanocomposites provides a sustainable approach to address structural integrity, electrical conductivity, catalytic activity, and stability concerns, thereby enhancing performance for the biosensing of uric acid (UA).[42] In addition to the surface moieties introduced by these carbon-based biomolecules, they also affect the electron transfer kinetics and the accessibility of the active site, directly improving the electrocatalytic detection of UA.[43] In order to improve the charge transfer rate, no attention has been paid to reducing the optical bandgap of NiO. It is possible to reduce the optical bandgap of NiO by tailoring the surface area and surface-active sites through the use of green-mediated approaches. Further reduced NiO, in terms of optical bandgap, can be combined with cobalt oxide to produce Co_3O_4/NiO composites for efficient enzyme-free sensing applications. The synthesis of Co_3O_4/NiO composite was based on the enriched transition metal ion variability obtained excellent redox performance during the sensitive detection of UA using electrochemical method. In addition to this, the easy synthesis, earth abundance and eco-friendly nature are the important factors in selecting a Co_3O_4/NiO hybrid system. These are the advantageous aspects for the fabrication of the Co_3O_4/NiO composite, which can be superior to other metal oxides. The purpose of this study is to report Co_3O_4/NiO composites using the juice of the *Cucumis melo* (Galia melon). The phytochemicals present in *Cucumis melo* juice include carbohydrates, dietary fibers, flavonoids, saponins, alkaloids, glycosides, and phenolic compounds.[44] In particular, phenolic compounds, carbohydrates, and flavonoids possess properties, such as structure-directing, reducing, capping, and stabilizing agents. Hence, the *Cucumis melo* was used to reduce the surface properties, shape, size, and surface area of NiO, resulting in a decrease in the optical bandgap of NiO. A method in which the optical bandgap of NiO is reduced using *Cucumis melo* and NiO is then combined with Co_3O_4 to build an enzyme-free UA sensor has not been reported previously in the literature. A non-enzymatic UA sensor based on a reduced Co_3O_4/NiO composite demonstrated ultra-high sensitivity, high catalytic oxidation capacity, selectivity, wide detection range, and low detection limit.

2 Materials and methods

2.1 Chemical reagents

The chemicals, including nickel chloride hexahydrate, 30% aqueous ammonia solution, uric acid, cobalt chloride hexahydrate, disodium phosphate, monopotassium phosphate, urea, glucose, potassium chloride, sodium hydroxide, and ascorbic acid, were procured in analytical grade from Sigma Aldrich, Karachi, Sindh, Pakistan. These chemicals were utilized in their received form, without further purification. A 0.1 M phosphate buffer solution (PBS) was prepared using deionized (D.I.) water, serving as the base for the uric acid (UA) solution employed in electrochemical characterization for UA detection.

2.2 Green-mediated synthesis of NiO nanoparticles *via* the modified hydrothermal method

A modified hydrothermal method was used to synthesize nickel oxide nanostructures (95 °C, 5 h), followed by a thermal

Scheme 1 Synthesis of reduced NiO and the reduced Co_3O_4/NiO composite using NiO by the hydrothermal method.

annealing process at 500 °C for 5 h.[45,46] Nickel oxide (NiO) samples were prepared by dissolving 0.1 M nickel chloride hexahydrate in 300 mL of deionized water, followed by the gradual addition of 5 mL of 33% aqueous ammonia. Ammonia was used to induce hydroxide ions in the growth solution for the formation of metal hydroxide. For the green-mediated synthesis, two separate beakers were prepared, each containing 0.5 mL and 1 mL of *Cucumis melo* juice, respectively, and labelled as reduced NiO-1 and reduced NiO-2. All beakers were sealed with aluminium foil to prevent contamination. The resulting light-green nickel hydroxide precipitates were vacuum-filtered, thoroughly washed with deionized water, and dried overnight. The final conversion of nickel hydroxide to NiO was achieved by calcination at 500 °C for 5 hours in ambient air. A pristine NiO (control) sample was synthesized using the same procedure but without the addition of bio-additives.

2.3 Synthesis of the Co_3O_4/NiO composite *via* the hydrothermal method

The synthesis of the reduced Co_3O_4/NiO composites involved the addition of 0.3 g and 0.5 g of reduced NiO (prepared as described in Section 2.2) into 0.1 M cobalt chloride hexahydrate ($CoCl_2 \cdot 6H_2O$). This was followed by the gradual addition of 5 mL of concentrated ammonia solution under vigorous stirring. For reference, Co_3O_4 precursors were produced using 0.1 M cobalt chloride hexahydrate and 5 mL of ammonia with a total volume of 100 mL of growth solution. To promote composite growth, the reaction mixtures were sealed with aluminum foil and heated at a temperature below 95 °C for 4 hours. The resulting material was subsequently vacuum filtered, thoroughly rinsed with deionized (D.I.) water, and dried overnight. Calcination at 500 °C for 7 hours facilitated the deposition of Co_3O_4 onto NiO, yielding the composite material and bare Co_3O_4. For comparison, a pure Co_3O_4/NiO composite (without *Cucumis melo* juice) was synthesized using pure NiO, as prepared in Section 2.2, following the same procedure. This method consistently produced high-quality Co_3O_4/NiO nanocomposite particles (NCPs), demonstrating its effectiveness for sustainable nanomaterial fabrication. A schematic of the phytochemical-mediated synthesis of the Co_3O_4/NiO composite is provided in Scheme 1.

2.4 Non-enzymatic electrochemical detection of UA using the Co_3O_4/NiO composite

The electrochemical characterization of the Co_3O_4/NiO composite for non-enzymatic uric acid (UA) detection was conducted using cyclic voltammetry (CV), chronoamperometry, linear sweep voltammetry (LSV), and electrochemical impedance spectroscopy (EIS). These measurements were performed in a standard three-electrode system, comprising a glassy carbon working electrode (GCE) with an area of 3 mm, a silver–silver chloride reference electrode (Ag/AgCl, 3 M KCl), and a platinum (Pt) wire counter electrode. The area of GCE was 0.013 cm^2. The GCE was polished with alumina paste, followed by a polishing cloth, and rinsed thoroughly with deionized water. The cleaned GCE was modified with a homogeneous ink of ultrasonically dispersed approximately 5 mg of NiO or Co_3O_4/NiO composites and 50 μL of 5% Nafion in 6 : 4 v/v (6 mL isopropyl alcohol and 4 mL methanol). Then, the drop casting method was used to deposit 5 μL of material ink on the cleaned GCE, which was then dried by blowing air at room temperature. A loading mass of approximately 20 μg cm^{-2} was deposited onto GCE. The modified GCE was dried by blowing air at room temperature. A 0.05 M uric acid (UA) stock solution was prepared in a 0.1 M phosphate buffer (PBS) at pH 7.3. Selectivity was evaluated by testing against 1.0 mM interferents, including ascorbic acid, urea, glucose, and electrolyte ions, in UA-spiked PBS. The linear range and limit of detection (LOD) were established based on findings from a previous study.[47]

2.5 Structural characterization

Various analytical methods, including powder X-ray diffraction (XRD), scanning electron microscopy (SEM), Fourier transform infrared (FTIR) spectroscopy, and UV-visible spectrometry, were employed to examine the NiO and Co_3O_4/NiO composites in terms of their crystalline structure and purity, morphology,

functional groups, and optical bandgap. The XRD patterns of the composites were obtained using a Bruker-D8 Advance ECO diffractometer. The chemical bonding characteristics were analysed with an FTIR spectrophotometer. The optical properties of the composites were investigated using a Shimadzu UV-2900 spectrometer within the wavelength range of 200–700 nm. The morphology of the Co_3O_4/NiO composites was studied *via* scanning electron microscopy (SEM) with an EVO18-CARL ZEISS instrument.

3 Results and discussion

3.1 Crystal, functional group, optical and morphological analysis of the synthesized materials

The crystal structure, phase, and purity of the pure NiO, pure Co_3O_4, reduced NiO-1, reduced NiO-2, pure Co_3O_4/NiO, reduced Co_3O_4/NiO-1 and reduced Co_3O_4/NiO-2 composites were analyzed using the powder XRD technique. Fig. 1a shows the distinctive diffraction patterns of the cubic phase in pure NiO, which align with the standard (JCPDS card no: 03-065-6920).[48,49] The reduced NiO nanostructures, synthesized using 0.5 mL and 1.0 mL of *Cucumis melo* juice, exhibited a slight decrease in diffraction pattern intensity, indicating the influence of the phytochemicals from *Cucumis melo*. These phytochemicals likely altered the crystal growth kinetics, affecting the size and shape of the NiO nanostructures and consequently reducing the intensity of the diffraction patterns. Fig. 1b shows the XRD patterns for pure Co_3O_4, which align well with the standard patterns of Co_3O_4 (JCPDS 01-074-2120)[50,51] and describe its cubic phase. The XRD patterns of the reduced Co_3O_4/NiO-1 and 2 composites are presented in Fig. 1b. Both composites displayed the characteristic cubic phases of NiO and cobalt oxide, confirming the successful formation of Co_3O_4/NiO composites with excellent crystalline properties (Fig. 1b). The absence of impurities or additional phases in the XRD analysis ensured the structural purity of the synthesized nanomaterials.[52–54] To identify the chemical bonding of metal–oxygen and various functional groups, the FTIR spectra of the NiO nanostructure and Co_3O_4/NiO composites were measured at room temperature. Literature indicates that the FTIR spectra of pure NiO typically display a distinct Ni–O stretching peak in the range of 400–700 cm^{-1}.[55] The FTIR spectra for pure NiO, pure Co_3O_4, and reduced NiO-1 and 2 composites are presented in Fig. 2a. Various IR bands were observed at frequencies such as 478 cm^{-1}, 550 cm^{-1}, 810 cm^{-1}, 1387 cm^{-1}, 1429 cm^{-1}, 2224 cm^{-1}, 3458 cm^{-1}, and 3621 cm^{-1}. Slight shifts in the IR bands may be attributed to differences in the hydrothermal conditions, as well as variations in the size and shape of the materials (Fig. 2a). Additional peaks appeared for reduced NiO-1 at 297 cm^{-1}, 701 cm^{-1} and 604 cm^{-1}. The IR bands at 487 and 667 cm^{-1} were attributed to NiO, while the bands at 3621 cm^{-1} and 1429 cm^{-1} were ascribed to surface-adsorbed hydroxyl groups from moisture. The band at 2224 cm^{-1} was likely due to atmospheric carbon dioxide. Other IR bands were assigned to functional groups derived from the growth precursors and phytochemicals of *Cucumis melo*. In the fingerprint region (500–1000 cm^{-1}), altered absorption bands confirmed the formation of Co_3O_4/NiO core–shell heterostructures, demonstrating synergistic effects due to changes in M–O (M = Co and Ni) stretching vibrations and interfacial charge transfer (Fig. 2b). The IR bands observed for the composite materials, as shown in Fig. 2b, included 425 cm^{-1}, 531 cm^{-1}, 903 cm^{-1}, 1387 cm^{-1}, 1517 cm^{-1}, 2228 cm^{-1}, and 3613 cm^{-1}. The IR bands at 425 and 531 cm^{-1} indicated metal–oxygen stretching vibrations, consistent with previous studies.[54,55] Slight variations in the IR bands for the composite materials (Fig. 2b) suggested the influence of synthetic conditions, crystal structure, and shape. The FTIR analysis confirmed the successful formation of the Co_3O_4/NiO composites, fully supporting the XRD results.

To evaluate the effect of *Cucumis melo* on the optical bandgap of NiO, UV-visible absorbance spectra were recorded for pure NiO and green-mediated NiO synthesized using 0.5 mL and 1 mL of *Cucumis melo* (reduced NiO-1 and 2), as shown in the SI (Fig. S1). *Cucumis melo*, which contained a wide range of phytochemicals, was expected to alter the morphology, size, and surface area of NiO, thereby modulating the optical bandgap.

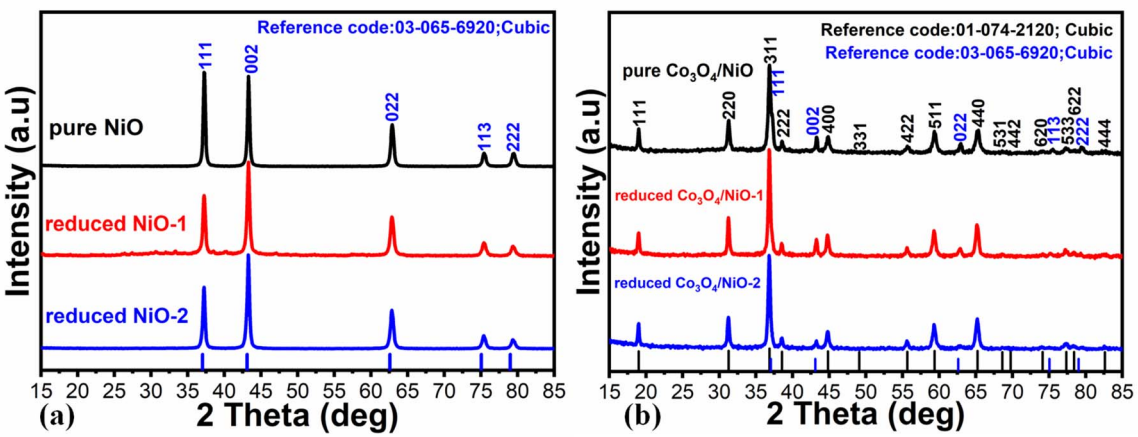

Fig. 1 (a) Powder reflections of the pure NiO nanostructures and reduced NiO nanostructures and (b) pure Co_3O_4/NiO and the reduced Co_3O_4/NiO composites.

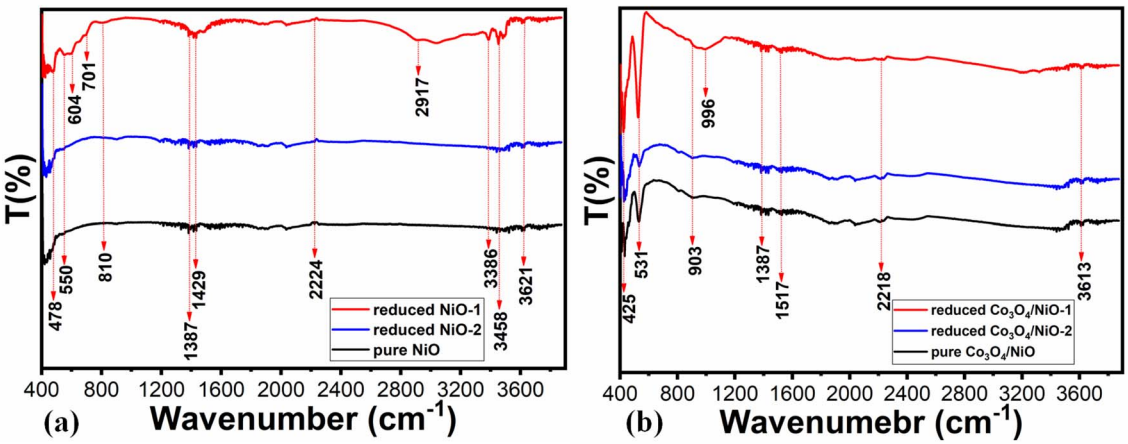

Fig. 2 (a) FTIR spectra of pure NiO and the reduced NiO nanostructures. (b) FTIR spectra of pure Co_3O_4/NiO and the reduced Co_3O_4/NiO composites.

This modulation, driven by changes in particle size, surface area, and structure, was anticipated to enhance charge transfer kinetics and improve the electrochemical activity of NiO. The UV-visible absorbance spectra for pure Co_3O_4/NiO composite and reduced Co_3O_4/NiO composites are presented in the SI (Fig. S1). Shoulder peaks in the UV-visible absorbance spectra were observed between 200 and 600 nm. A peak attributed to exciton transitions was identified around 300–350 nm for all the synthesized nanomaterials.[56] The Tauc's plots were used to determine the optical band gap values for each material, as shown in Fig. S1. The optical band gap values were 3.10 eV, 2.66 eV, and 2.98 eV for pure NiO, reduced NiO-1, and reduced NiO-2, respectively (Fig. 3c). The composite materials, including pure Co_3O_4/NiO and reduced Co_3O_4/NiO-1 and 2 composites, showed optical bandgap values of 2.58 eV, 2.07 eV and 2.38 eV, respectively, as shown in Fig. S1. The alteration in the optical bandgap values can be attributed to variations in surface morphology, particle size, and structural defects (easier removal of electrons), possibly because of higher charge density (more electron clouds) and reduced binding energies due to a variation in the oxidation state and the synthetic method employed.[57] SEM analysis was conducted to examine the morphology of the synthesized materials. The SEM micrographs of the pure NiO, reduced NiO-1 and 2 synthesized using 0.5 mL and 1 mL of *Cucumis melo*, pure Co_3O_4, pure Co_3O_4/NiO composite, and reduced Co_3O_4/NiO-1 and reduced Co_3O_4/NiO-2 composites are presented in Fig. 3. Pure NiO exhibited a sheet-like morphology with a lateral size of around 100 nm and a thickness of less than 20 nm (Fig. 3a). The sheet structures were uniform throughout the sample. The use of *Cucumis melo* juice induced significant morphological changes (Fig. 3b and c). Although the sheet structure was retained, the sample appeared as densely packed particles for reduced NiO-1 synthesized with 0.5 mL of *Cucumis melo* (Fig. 3b), while when 1 mL of *Cucumis*

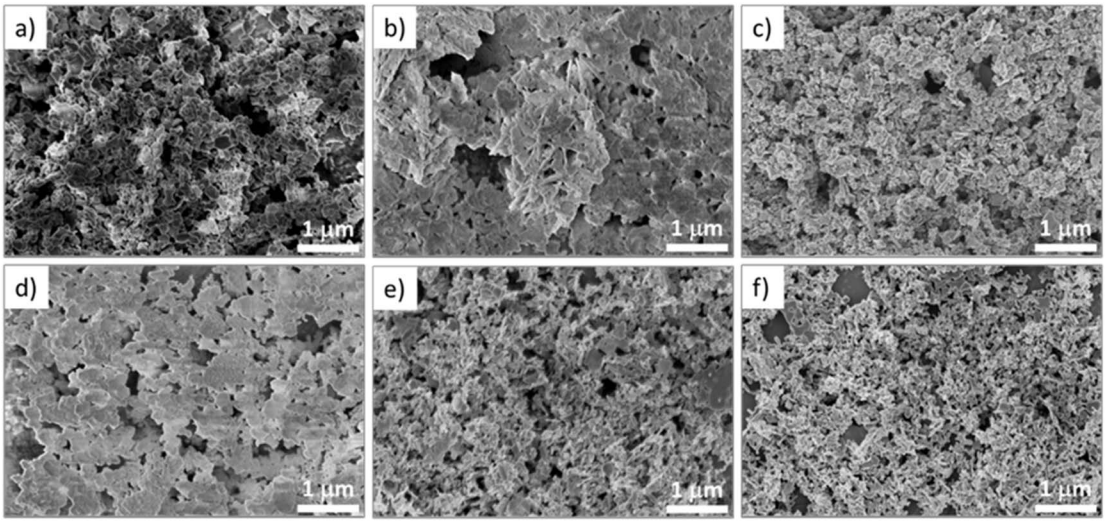

Fig. 3 SEM images of (a) pure NiO, (b) reduced NiO-1 synthesized using 0.5 mL of *Cucumis melo*, (c) reduced NiO-2 synthesized using 1 mL of *Cucumis melo*, (d) pure Co_3O_4/NiO composite, (e) reduced Co_3O_4/NiO-1 composite using 0.5 mL of *Cucumis melo* and f) reduced Co_3O_4/NiO-2 composite synthesized using 1 mL of *Cucumis melo*.

melo was used, the nanoparticles resembled those observed for pure NiO (Fig. 3c). The phytochemicals from *Cucumis melo*, such as phenolic compounds, carbohydrates, and flavonoids, played the role of reducing, stabilizing, and structure-directing agents during the growth of NiO; thus they together modified the size and surface properties. Compared to the pure Co_3O_4/NiO composite (Fig. 3d), the reduced Co_3O_4/NiO composites revealed much smaller particles, indicated by SEM analysis, particularly in the reduced Co_3O_4/NiO-1 composite prepared with 0.3 g reduced NiO-1 using 0.5 mL of *Cucumis melo* (Fig. 3e and f). Overall, the SEM study evidenced morphological modifications, particularly a significant reduction in size, after the chemical modification was observed, *e.g.* for the composite materials. The resulting enhancement in the surface was expected to positively impact their electrochemical performance. The bare Co_3O_4 experienced a typical nanorod-like morphology of nanoparticles, as shown in SI (Fig. S2). The length of nanorods could be several microns, and the size of assembled nanoparticles could be less than 200 nm.

3.2 Electrochemical oxidation of UA using the non-enzymatic sensing approach on the Co_3O_4/NiO composite

The modified GCE, incorporating pure NiO and Co_3O_4, reduced NiO-1 and 2, pure Co_3O_4/NiO composite, and reduced Co_3O_4/NiO-1 and 2 composites, was used as the working electrode in a three-electrode cell setup, with 0.1 M PBS (pH 7.3) as the electrolyte. CV analysis was conducted on bare GCE, pure NiO and Co_3O_4, reduced NiO-1 and 2, and pure Co_3O_4/NiO composite, as well as reduced Co_3O_4/NiO-1 and 2 composites, at a scan rate of 50 mV in a 0.5 mM UA solution (Fig. 4a). The electrochemical activities were highly dependent on the method of preparation and the growth conditions. Pure NiO and bare GCE exhibited no significant electrochemical activity, whereas reduced NiO-1 and 2 demonstrated oxidative properties due to surface modifications through the phytochemicals from *Cucumis melo*, which contained proteins, polyphenols and flavonoids that reduced the size, yielded a sheet-like shape, and enhanced catalytic properties. Reduced NiO showed slightly higher electrochemical performance in UA oxidation. The pure Co_3O_4/NiO composite exhibited lower redox characteristics compared to pure Co_3O_4 during UA oxidation, whereas the reduced Co_3O_4/NiO-1 composite (best sample) exhibited excellent oxidizing properties, making it the most efficient electrocatalytic material in this study. Combining reduced NiO with Co_3O_4 in the fabrication of the reduced Co_3O_4/NiO composite provided abundant surface-active sites, favorable morphology, rapid charge transfer kinetics, and a synergistic effect, enhancing electrochemical performance. The preliminary CV analysis

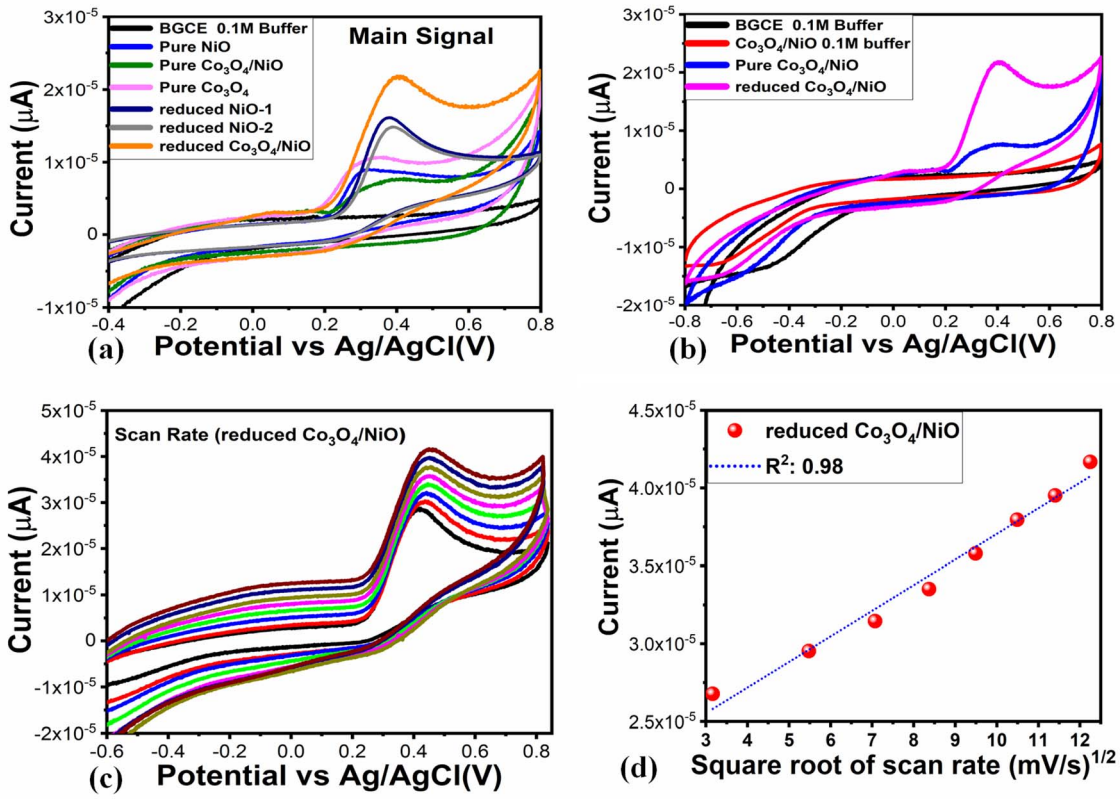

Fig. 4 (a) Main signal CV curves of pure NiO and the reduced NiO-1 and 2 nanostructures in 0.1 M PBS at pH 7.3 and a scan rate of 50 mV s^{-1}, (black) bare GCE only in a phosphate buffer solution, pure NiO (blue), reduced NiO-1 (navy), and reduced NiO-2 (gray) in 0.5 mM UA prepared in 0.1 M PBS at pH 7.3, pure Co_3O_4/NiO (olive), pure Co_3O_4 (light magenta), and Co_3O_4/NiO-1 (orange) in 0.5 mM UA prepared in 0.1 M PBS at pH 7.3. (b) CV curves of pure Co_3O_4/NiO, the reduced Co_3O_4/NiO-1 composite, and the reduced Co_3O_4/NiO-2 composite in 0.1 M PBS at pH 7.3 and a scan rate of 50 mV s^{-1} (c) CV curves of the reduced Co_3O_4/NiO composite at various scan rates in 0.5 mM UA prepared in 0.1 M PBS at pH 7.3. (d) Linear plot of oxidation peak current against different scan rates.

revealed that the electrochemical performance of the materials highly depended on the shape, size, structure, and surface active sites. To further analyze the electrochemical performance of the reduced Co_3O_4/NiO composite, it was tested in 0.1 M PBS (pH 7.3) and compared with the pure Co_3O_4/NiO composite in the electrolytic solution (Fig. 4b). This analysis revealed negligible electrolyte contribution, while the response of the reduced Co_3O_4/NiO composite in 0.5 mM UA showed that the oxidation peak primarily resulted from UA oxidation. This preliminary CV analysis confirmed the high potential of the reduced Co_3O_4/NiO composite for non-enzymatic sensing applications. Consequently, the charge transfer kinetics of the composite was studied *via* scan rate analysis, and its working range for the UA sensor, stability, selectivity, and real-sample applications were determined. The scan rate analysis of the reduced Co_3O_4/NiO composites at varying scan rates in a 0.5 mM UA solution (Fig. 4c) showed a linear increase in oxidation peak current without a proper reduction peak, indicating the electrode's irreversible behavior. Incremental increases in the scan rate shifted the peak potential toward more positive values due to sluggish charge transfer or solution resistance, resulting in slow reaction kinetics.[58] High scan rates increased the peak current and introduced an ohmic potential drop due to solution resistance. The magnitude of the ohmic drop increased significantly with high scan rates as the peak current increased (Fig. 4c). The oxidation peak current was plotted against the square root of the scan rates (Fig. 4d), revealing a linear fit with a regression coefficient of 0.99. This confirmed the excellent diffusion-controlled properties of the modified electrode and its suitability for controlled charge transfer kinetics. The electrocatalytic oxidation of UA ($C_5H_4N_4O_3$) underwent a 2-electron, 2-proton oxidation to form allantoin ($C_4H_6N_4O_3$), as given below:

$$C_5H_4N_4O_3 + 2H_2O \rightarrow C_4H_6N_4O_3 + CO_2 + 2H^+ + 2e^-. \quad (1)$$

Here, in the reduced Co_3O_4/NiO composite, the presence of mixed oxidation states of (Co^{+2}/Co^{+3}) was observed. Further, Co_3O_4 functioned as an active catalyst in the UA sensor, thereby ensuring UA oxidation, while NiO offered a stable matrix with a high surface area for increasing the stability of Co_3O_4, thereby guaranteeing the uniform dispersion of Co_3O_4 and avoiding agglomeration. The UA sensing mechanism is briefly described in Scheme 2.

3.3 Working range, stability and selectivity studies of the Co_3O_4/NiO-1 composite

Various electrochemical modes were employed to evaluate the performance of the proposed non-enzymatic UA sensor based on the Co_3O_4/NiO composite, as depicted in Fig. 5a. Cyclic voltammetry (CV) was conducted on the Co_3O_4/NiO composite at a scan rate of 50 mV s^{-1}, utilizing different concentrations of UA in PBS (pH 7.3) to establish the sensor's linear range. The sensor demonstrated a wide detection range for UA, spanning from 0.5 mM to 16 mM, as shown in Fig. 5a. A linear response was observed, with increasing oxidation peak currents, corresponding to the successive additions of UA, effectively aligning the potential of the Co_3O_4/NiO composite for UA detection. Notably, the significant current generated at each UA concentration highlighted the sensor's sensitivity. A slight shift in peak potential was noted with the addition of UA, potentially due to slow charge transfer kinetics and ohmic drop. The linearity of the sensor was further confirmed by plotting oxidation peak currents against UA concentrations, yielding a regression coefficient of 0.99, as shown in Fig. 5b. This indicated the sensor's accurate analytical performance. The exceptional linear range

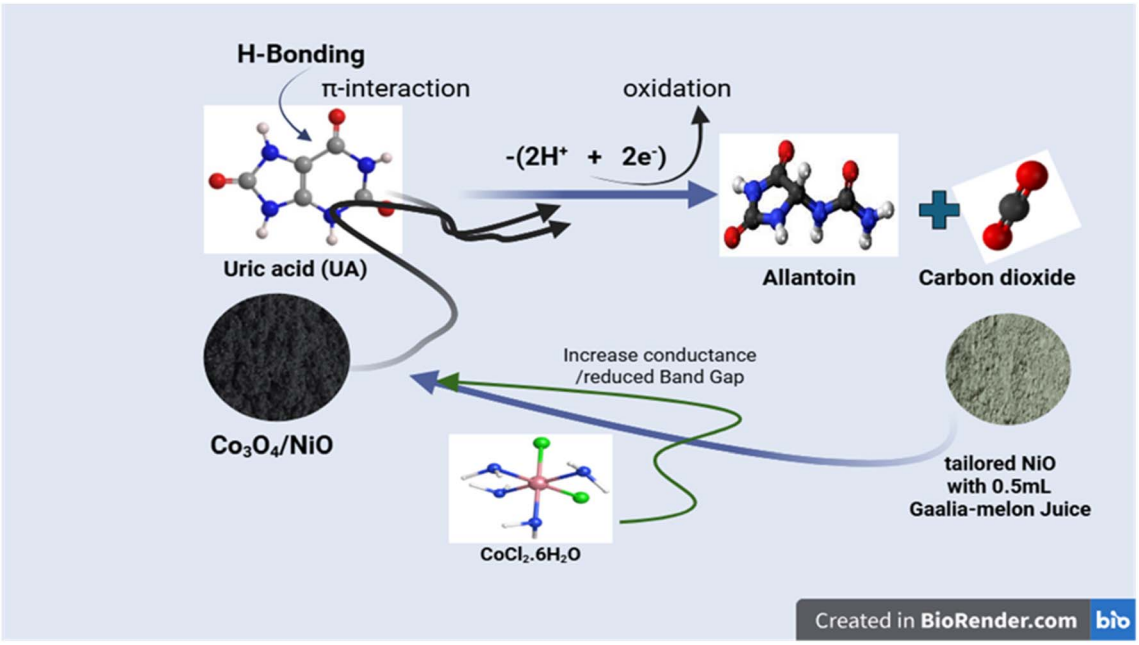

Scheme 2 Reaction mechanism of the oxidation of uric acid on the Co_3O_4/NiO electrode.

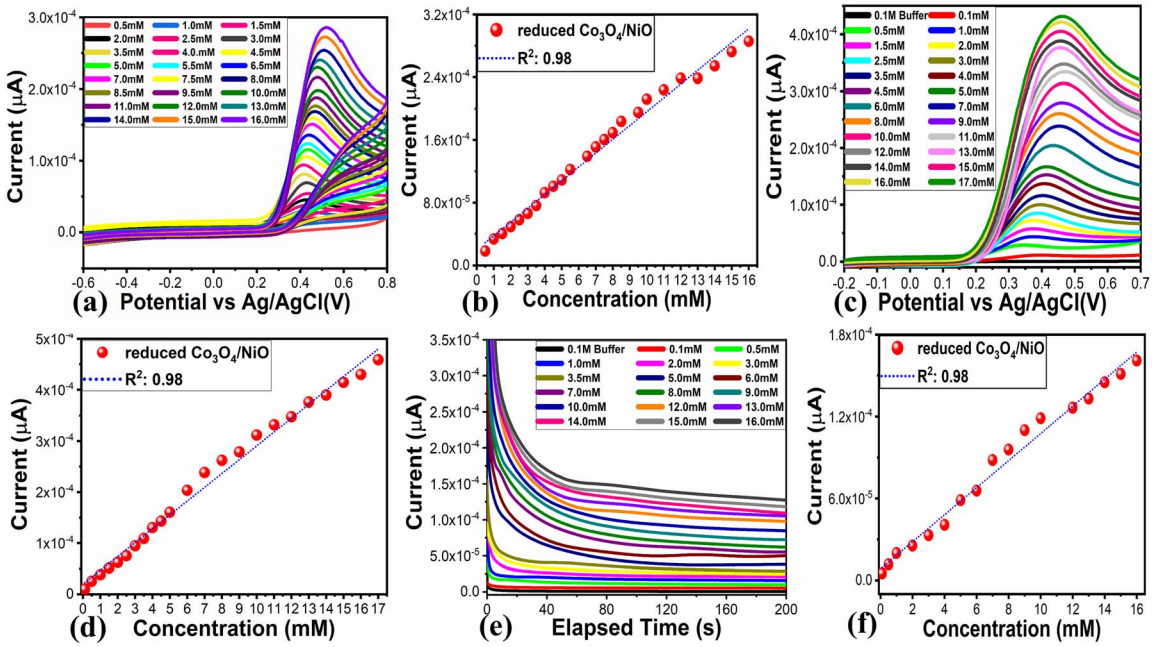

Fig. 5 (a) CV curves at a scan rate of 50 mV s^{-1} for the reduced Co_3O_4/NiO composite at various UA concentrations in 0.1 M PBS at pH 7.3. (b) Linear plot of the uric acid oxidation peak current against different UA concentrations. (c) Linear sweep voltammetric curves at a scan rate of 50 mV s^{-1} for the reduced Co_3O_4/NiO composite in the presence of various concentrations of UA in prepared 0.1 M PBS at pH 7.3. (d) Linear plot of the peak current *versus* successive increase in UA concentrations. (e) Chronoamperometric response curves of the reduced Co_3O_4/NiO composite at a fixed potential of 0.4 V *versus* Ag/AgCl at various UA concentrations prepared in 0.1 M PBS at pH 7.3. (f) Linear plot of the rising current of each chronoamperometric response curve *versus* corresponding UA concentration.

of the proposed non-enzymatic UA sensor could be attributed to the modified surface, increased catalytic sites, fast charge transfer kinetics, and stabilized reduced Co_3O_4/NiO composite matrix. The reduced NiO component contributed to a decline in the optical bandgap through modifications in size, shape, surface area, and defects, achieved *via* a green-mediated approach. This approach enhanced electron transfer conductance and provided a wide range of surface and size properties. Additionally, the combination of reduced NiO with Co_3O_4 amplified the catalytic sites, improved charge transport, and stabilized the Co_3O_4/NiO composite, resulting in excellent electrochemical performance for the non-enzymatic oxidation of UA. The working range of the sensor was determined using LSV at a scan rate of 50 mV s^{-1}, with successive additions of UA in the electrochemical cell. LSV curves (Fig. 5c) revealed a wide detection range (0.1–17 mM) due to the unique matrix of the reduced Co_3O_4/NiO composite, which facilitated sensitive UA detection. A linear plot (Fig. 5d) was obtained by plotting the peak current against UA concentrations, showing a regression coefficient of 0.99, indicating excellent analytical performance. Chronoamperometric analysis at 0.4 V *vs.* Ag/AgCl (Fig. 5e) confirmed a linear increase in the current with the UA concentration, with another linear plot (Fig. 5f) yielding a regression coefficient of 0.99. CV, LSV, and chronoamperometric methods verified the sensor's wide linear range and high accuracy, making it a promising analytical tool. The sensitivity was calculated through a linear regression equation with normalization by electrode area under the following expression:

$$s = \frac{\Delta I/A}{\Delta C},$$

$$I/A = m \times C + b,$$

where S = sensitivity, I = measured current (uA), A = working electrode area (0.013 cm^2), C = analyte concentration (mM), m = normalised slope, b = normalised intercept.

The sensitivity of the reduced Co_3O_4/NiO composite was evaluated at 7.63 × 10^{-4} μA mM^{-1} cm^{-2} over the linear range from 0.1 mM to 16 mM.[59,60] However, the limit of detection (LOD) and limit of quantification (LOQ) were examined by the chronoamperometry method using the following expressions:

$$\mathrm{LOD} = 3.3\ \mathrm{SD}/S,$$

$$\mathrm{LOQ} = 10\ \mathrm{SD}/S.$$

The sensitivity (S) of the proposed UA sensor and the standard deviation (SD) are key parameters. The estimated chronoamperometric LOD and LOQ values were 0.005 mM and 0.008 mM, respectively. The low LOD highlighted the potential of the Co_3O_4/NiO composite-based non-enzymatic UA sensor for monitoring elevated UA levels in human fluids. Keeping in view the rapid and sensitive nature of the chronoamperometric method, the proposed study suggested it as a primary sensing method for the non-enzymatic detection of UA. The normal

range of blood serum is 0.15–0.48 mM. In the urine, the normal excretion of UA is 1.48 to 4.43 mM per 24 h. These are clinical observations about the presence of UA in the urine and blood serum samples under normal conditions. The proposed method showed a wide linear range, indicating the efficiency of the method to detect UA in the normal range and above. This could be used for a patient having high UA levels, if we see it from a clinical point of view. This is the reason behind the high linear range that is attributed to the efficiency of the designed material for sensing UA. In our study, we aim to design a material configuration that exhibits high electrocatalytic performance; thus, we are demonstrating a material that is highly applicable for the detection of UA in patients who suffer from high UA levels. The selectivity of a non-enzymatic UA sensor is very critical for confirming the applicability of the sensor in the environment of competing interfering agents. For this reason, we measured separate CV curves for each interfering agent at the scan rate of 50 mV s^{-1}. Selectivity was assessed *via* CV (Fig. 6a), showing negligible peak current variation in the presence of the interfering agents (ascorbic acid, urea, glucose, sodium, potassium, and magnesium ions at 0.1 mM with 1 mM UA in PBS, pH 7.3). These observations were shown by the CV curves during selectivity analysis, indicating that the proposed sensor showed only the well-resolved oxidation peak for UA; however, there was no significant oxidation peak in the CV curves for the common interfering agent, as shown in Fig. 6a. Stability was evaluated through 16 consecutive CV cycles, as shown in Fig. S3, showing minimal peak current and potential changes. Reproducibility, as shown in Fig. S3, demonstrated less than 5% deviation in the oxidation peak current, confirming excellent reproducibility. The long-term stability of the reduced Co_3O_4/NiO composite-based UA sensor was investigated for the period of 60 h using the chronoamperometry method at approximately 0.4 V *vs.* Ag/AgCl using 0.5 mM UA, as shown in Fig. 6b. For studying the long-term stability, a reported research work was followed.[61] It could be seen that the proposed sensor did not show any significant fluctuation in the current and remained very durable for the period of 60 h; hence, it could be used for long-term applications.

To investigate the electrochemically active surface area (ECSA) of the synthesized nanocomposites, the double-layer capacitance (C_{dl}) was determined based on the non-Faradic behavior of the CV curves at various scan rates in 0.1 M PBS medium, as shown in Fig.S4. The electrochemical performances of pure NiO, reduced NiO-1 and 2, pure Co_3O_4/NiO composite and reduced Co_3O_4/NiO composite were analyzed using non-Faradic CV curves at different scan rates. The CV curves for all materials, as shown in Fig. S4, exhibited a typical non-Faradic response across a wide range of scan rates. Linear plots (Fig. 7a) were constructed by calculating the difference between anodic and cathodic current densities at each scan rate, with the slope representing C_{dl}. The C_{dl} values for pure NiO, reduced NiO-1 and 2 were 1.4, 1.9, and 1.8 μF cm^{-2}, respectively. For pure Co_3O_4/NiO and reduced Co_3O_4/NiO composites, the linear plots are shown in Fig. 7b. The corresponding C_{dl} values of these composite systems were 1.8 and 4.0 μF cm^{-2}, respectively. Further, to precisely calculate the ECSA values, we used the following formula:[62,63]

$$\mathrm{ECSA} = C_{dl}/C_{specific},$$

where $C_{specific}$ is the specific capacitance.

The ECSA values for pure NiO, reduced NiO-1 and 2, pure Co_3O_4/NiO and reduced Co_3O_4/NiO composite were 35 cm^2 g^{-1}, 47.5 cm^2 g^{-1}, 45.1 cm^2 g^{-1}, 45.5 cm^2 g^{-1} and 100 cm^2 g^{-1}, respectively. The reduced Co_3O_4/NiO composite demonstrated a significantly high active surface area, making it suitable for the sensitive detection of UA.

Understanding charge transfer kinetics is essential for elucidating the improved electrochemical performance of electrocatalytic materials. All synthesized materials were evaluated through EIS measurements across a frequency range from 0.1 Hz to 100 kHz, with an amplitude of 5 mV and a biasing potential set to the oxidation potential of UA (0.4 V). The raw EIS data were fitted using a distinctive equivalent circuit, including elements such as internal resistance (R_s),[62] charge transfer resistance (R_{ct}), and constant phase element (CPE).[63] After the fitting of the EIS data, the corresponding

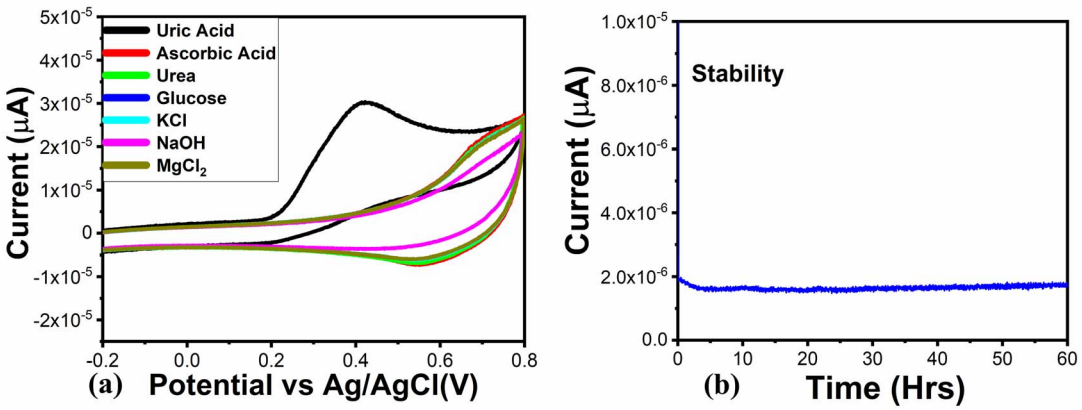

Fig. 6 (a) Selectivity *via* measuring different CV curves at a scan rate of 50 mV s^{-1} for the reduced Co_3O_4/NiO composite in 1.0 mM UA prepared in 0.1 M PBS at pH 7.3 and other possible interfering substances having a concentration of 0.1 mM during the sensing of UA. (b) Chronoamperometric response at 0.4 V *vs.* Ag/AgCl in 0.5 mM UA for the period of 60 h.

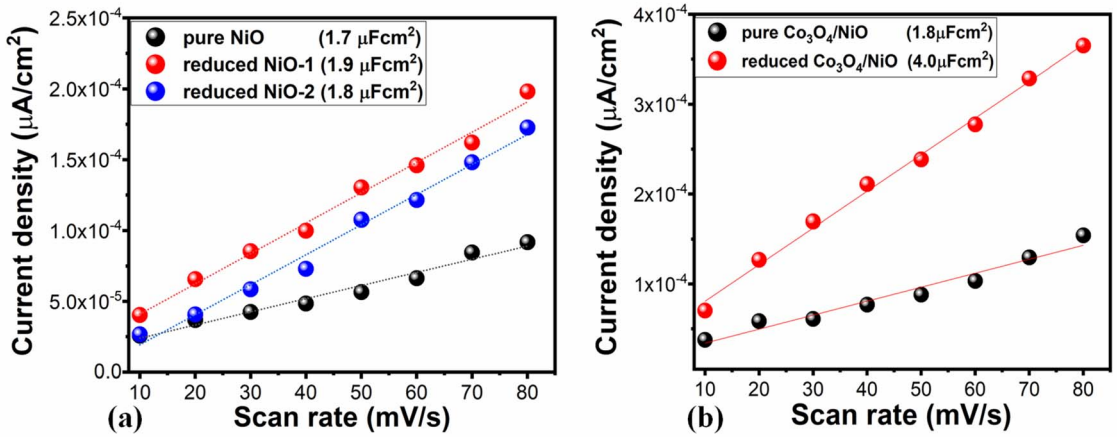

Fig. 7 (a) and (b) Linear plots of anodic current density difference for each scan rate for the quantification of ECSA.

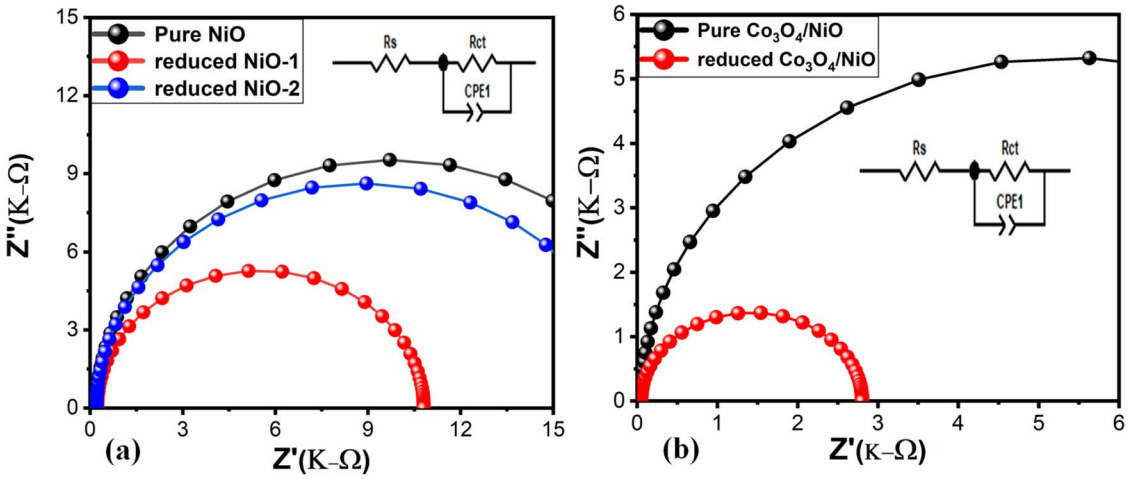

Fig. 8 (a) and (b) Nyquist plots obtained for pure NiO, the pure Co_3O_4/NiO composite, reduced NiO-1/2 composite and reduced Co_3O_4/NiO-1 composite in 1.0 mM UA prepared in 0.1 M PBS at pH 7.3 by EIS fitted data; inset: fitted circuits with defined elements, such as solution resistance (R_s), charge transfer resistance (R_{ct}), and constant phase element double layer (CPEdl).

Nyquist plots of pure NiO, reduced NiO-1 and 2, pure Co_3O_4/NiO composite, and reduced Co_3O_4/NiO composite are shown in Fig. 8a and b. It could be seen from the Nyquist plots that the Co_3O_4/NiO composite possessed the lowest charge transfer resistance (R_{ct}) compared to other materials. The charge transfer resistance (R_{ct}) values of 19 062 Ohm, 9476 Ohm, 10 572 Ohm, 10 660 Ohm, and 2751 Ohm were estimated for pure NiO, reduced NiO-1 and 2, pure Co_3O_4/NiO composite, and reduced Co_3O_4/NiO composite, respectively. The R_{ct} value is highly dependent on the nature of the electrolyte. Compared to other materials, the reduced Co_3O_4/NiO composite experienced a relatively low R_{ct} value, suggesting its favorable charge transfer kinetics at the interface of the electrode and electrolyte. The enhanced conductivity of an electrocatalytic material promotes electron mobility during the electrocatalytic reaction.[64] The EIS analysis revealed that the reduced Co_3O_4/NiO composite exhibited superior conductivity over other presented materials, which was caused by a number of accessible oxidation sites that increased charge carrier density and reduced electrical resistance, consequently providing an enhanced electrical signal during the oxidation of UA.

Table 1 Percentage recovery of the reduced Co_3O_4/NiO composites (sample 1) towards UA detection using a real sample and the standard addition method

Sample ID	Added UA (mM)	Found UA (mM)	% Recovery	RSD % ($n = 3$)
Blood-1	—	0.7	—	—
	1.0	1.68 ± 0.03	99	3.1 ± 0.4
	2.0	3.76 ± 0.04	102	4.4 ± 0.6
	3.0	5.89 ± 0.05	103	4.8 ± 0.3
Blood-2	—	0.6	—	—
	1.0	1.61 ± 0.04	101	3.21 ± 0.7
	2.0	3.73 ± 0.04	104	4.47 ± 0.9
	3.0	5.78 ± 0.05	103	4.4 ± 0.8

Table 2 Comparative analysis of the as-reported reduced Co_3O_4/NiO composite non-enzymatic sensing for UA against recently developed modified electrode materials

Sensing electrode material	Linear range (mM)	Limit of detection (mM)	References
ITO-rGO-AuNPs	0.01–0.5	0.003	67
Co_3O_4 nanoberries/GCE	0.005–3.0	0.002	68
Porous Co_3O_4/GCE	0.01–2.5	0.010	22
$NiCo_2O_4$NPs	0.1–8.0	0.005	69
Co_3O_4 puffyballs/GCE	0.01–1.5	0.002	70
CuNi-MoF@rGO	0.01–1.0	0.009	72
ZnS/RGO	0.01–2.0	0.048	73
Co_3O_4/NiO	0.1–16.0	0.005	This work

3.4 Real sample application

To evaluate the feasibility of the reduced Co_3O_4/NiO composite as a non-enzymatic UA sensor for detecting UA in blood serum samples using the standard addition method, the sensor was first employed to detect UA in blood serum.[65] Two blood samples were collected with the consent of two persons on the author's list. The serum from the whole blood sample was collected through the concentration process at room temperature. After the concentration, the top layer was collected using a pipette. Subsequently, various additions were made to the blood serum samples, and UA sensing was performed. The performance was assessed in terms of percent recovery (%) using the following formula:

$$\%\ \text{Recovery} = \frac{\text{amount of substrate added}}{\text{initial amount of substrate}} \times 100.$$

The calculated values of % recovery are given in Table 1. The results indicated excellent % recovery and low RSD, confirming the superior analytical performance of the reduced Co_3O_4/NiO composite-based non-enzymatic UA sensor for quantifying UA in real-world samples. However, there was a slight increase in the % recovery value due to the possible presence of other substances in the real blood serum samples. The overall performance of the as-presented electrocatalytic materials was highly structure, morphology, surface and size-dependent, and such aspects of material design have been reported.[66] The performance of the as-reduced Co_3O_4/NiO composite was compared with those of existing modified electrodes for the detection of UA, as given in Table 2.[67–73] It was clear that the presented electrocatalytic material was simple, low-cost, efficient and eco-friendly for the wide-range quantification of UA, and its performance was superior or comparable to those of many of the existing materials; hence, it could be used as an alternative material for the detection of UA in real-world samples.

4 Conclusions

In summary, the phytochemicals from *Cucumis melo* were utilized to modify the surface and structure of NiO, resulting in a reduction of its optical bandgap. NiO-1 with a reduced optical bandgap (2.07 eV) was combined with Co_3O_4 to form a reduced Co_3O_4/NiO-1 composite with an optical bandgap of 2.66 eV. The crystalline properties of the composite were analyzed using XRD, which confirmed the cubic phases of NiO and cobalt oxide, thereby validating the formation of the composite system. These findings were further supported by FTIR analysis. The electrochemical performance of the reduced Co_3O_4/NiO composite was evaluated for the non-enzymatic detection of UA in 0.1 M PBS (pH 7.3). The sensor demonstrated a wide linear detection range from 0.1 mM to 16 mM for UA using the chronoamperometric method, with a low detection limit (LOD) of 0.005 mM. The composite exhibited excellent stability and selectivity. The enhanced performance of the modified electrode was attributed to rapid charge transport, abundant catalytic sites, surface modification, favourable morphology, and the synergistic effect within the reduced Co_3O_4/NiO composite. The superior electrochemical performance of the composite highlighted its potential for integration into real-time biomedical devices and energy-related applications.

Ethical statement

All experiments related to human blood samples were performed in accordance with the Guidelines of the ethical committee of the University of Sindh, and the experiments were approved by the ethical committee of the University of Sindh, Jamshoro, Sindh, Pakistan. Informed consents were obtained from the human participants of this study.

Author contributions

Arslan Uddin Qureshi: material synthesis and partial electrochemical tests. Humaira Khan: supervision. Aneela Tahira: XRD analysis. Shaista Bano Memon: real sample preparation and analysis. Asma Hayat: UV-visible measurements. Saba Naz: optical bandgap analysis. Muhammad Ali Bhatti: EIS analysis. Aftab Ahmed Khand: sensor performance evaluation. Matteo Tonezzer: XRD measurements. Brigitte Vigolo: SEM analysis. Elmuez Dawi: result visualization and draft editing. Rafat M. Ibrahim: validation of the results and editing of the draft. Zafar Hussain Ibupoto: supervision, conceptualization of the study and writing of the original draft of the manuscript.

Conflicts of interest

The authors have no conflicts and competing interests in the presented research work.

Data availability

The authors declare that the data supporting the findings of this study are available within the paper.

Supplementary information (SI): the morphology of Co_3O_4,-Optical bandgap, reproducibility of the modified electrode and current density at various scan rate of synthesized materials. See DOI: https://doi.org/10.1039/d6ra01598k.

Acknowledgements

The authors acknowledge the Pakistan Science Foundation and the Natural Science Foundation, China, for partially supporting the project, PSF-NSFC/202307/427. The authors would also like to acknowledge the partial support received from Ajman University, Internal Research Grant No. [DRG ref. 2025-IRG-CHS-04]. We acknowledge the CeSAR (Centro Servizi d'Ateneo per la Ricerca) of the University of Cagliari, Italy, for the XRD measurements.

References

1 M. Kuwabara, *et al.*, Current updates and future perspectives in uric acid research, 2024, *Hypertens. Res.*, 2025, **48**(2), 867–873.
2 T. Chu, *et al.*, *Uric Acid: A Biomarker and Pathogenic Factor of Affective Disorders and Neurodegenerative Diseases*, 2025, vol. 31, pp. 585–597.
3 L. N. Mileti and J. D. Baleja, The Role of Purine Metabolism and Uric Acid in Postnatal Neurologic Development, *Molecules*, 2025, **30**(4), 839.
4 L. Du, *et al.*, Hyperuricemia and its related diseases: mechanisms and advances in therapy, *Signal Transduct. Target. Ther.*, 2024, **9**(1), 212.
5 Y. M. Roman, *et al.*, The role of uric acid in human health: Insights from the uricase gene, *J. Pers. Med.*, 2023, **13**(9), 1409.
6 K. Ma, *et al.*, Electrochemical Sensor Nanoarchitectonics for Sensitive Detection of Uric Acid in Human Whole Blood Based on Screen-Printed Carbon Electrode Equipped with Vertically-Ordered Mesoporous Silica-Nanochannel Film, *Nanomaterials*, 2022, **12**(7), 1157.
7 Q. Yan, *et al.*, A highly sensitive uric acid electrochemical biosensor based on a nano-cube cuprous oxide/ferrocene/uricase modified glassy carbon electrode, *Sci. Rep.*, 2020, **10**(1), 10607.
8 Y. Wang, *et al.*, Electrochemical Sensors for Clinic Analysis, *Sensors*, 2008, **8**, 2043–2081, DOI: 10.3390/s8042043.
9 S. Verma, *et al.*, Uricase grafted nanoconducting matrix based electrochemical biosensor for ultrafast uric acid detection in human serum samples, *Int. J. Biol. Macromol.*, 2019, **130**, 333–341.
10 R. Ahmad, *et al.*, Solution Process Synthesis of High Aspect Ratio ZnO Nanorods on Electrode Surface for Sensitive Electrochemical Detection of Uric Acid, *Sci. Rep.*, 2017, **7**(1), 46475.
11 R. Abdel-Karim, Y. Reda and A. Abdel-Fattah, Review—Nanostructured Materials-Based Nanosensors, *J. Electrochem. Soc.*, 2020, **167**(3), 037554.
12 R. Ahmad, *et al.*, Deposition of nanomaterials: A crucial step in biosensor fabrication, *Mater. Today Commun.*, 2018, **17**, 289–321.
13 R. Ahmad, *et al.*, Highly Efficient Non-Enzymatic Glucose Sensor Based on CuO Modified Vertically-Grown ZnO Nanorods on Electrode, *Sci. Rep.*, 2017, **7**(1), 5715.
14 R. G. Krishnan, R. Rejithamol and B. Saraswathyamma, Non-enzymatic electrochemical sensor for the simultaneous determination of adenosine, adenine and uric acid in whole blood and urine, *Microchem. J.*, 2020, **155**, 104745.
15 V. Nagal, *et al.*, Highly Sensitive Electrochemical Non-Enzymatic Uric Acid Sensor Based on Cobalt Oxide Puffy Balls-like Nanostructure, *Biosensors*, 2023, **13**(3), 375.
16 F. J. Sonia, *et al.*, Interface and Morphology Engineered Amorphous Si for Ultrafast Electrochemical Lithium Storage, *Small*, 2024, **20**(29), 2311250.
17 M. Pantrangi, *et al.*, Flexible micro-supercapacitors: Materials and architectures for smart integrated wearable and implantable devices, *Energy Storage Mater.*, 2024, **73**, 103791.
18 B. S. Dakshayini, *et al.*, Role of conducting polymer and metal oxide-based hybrids for applications in ampereometric sensors and biosensors, *Microchem. J.*, 2019, **147**, 7–24.
19 N. Abhishek, *et al.*, Metal-conducting polymer hybrid composites: A promising platform for electrochemical sensing, *Inorg. Chem. Commun.*, 2023, **157**, 111334.
20 Z. H. Mahmoud, *et al.*, Recent advances in the applications of smart nanomaterials in Biomedicine: A review, *Nano Life*, 2026, **16**(03), 2530005.
21 J. S. Han, *et al.*, Epoxy-Based Copper (Cu) Sintering Pastes for Enhanced Bonding Strength and Preventing Cu Oxidation after Sintering, *Polymers*, 2024, **16**(3), 398.
22 S. Masrat, *et al.*, Electrochemical Ultrasensitive Sensing of Uric Acid on Non-Enzymatic Porous Cobalt Oxide Nanosheets-Based Sensor, *Biosensors*, 2022, **12**(12), 1140.
23 Q. Wang, *et al.*, Electrophoretic Deposition of Co3O4 Particles/Reduced Graphene Oxide Composites for Efficient Non-Enzymatic H2O2 Sensing, *Materials*, 2023, **16**(3), 1261.
24 S. Ramesh, *et al.*, Cubic nanostructure of Co3O4@nitrogen doped graphene oxide/polyindole composite efficient electrodes for high performance energy storage applications, *J. Mater. Res. Technol.*, 2020, **9**(5), 11464–11475.
25 D. Zhang, *et al.*, MXene/Co3O4 composite based formaldehyde sensor driven by ZnO/MXene nanowire arrays piezoelectric nanogenerator, *Sens. Actuators, B*, 2021, **339**, 129923.
26 D. Zhang, *et al.*, Layer-by-Layer Self-assembly of Co3O4 Nanorod-Decorated MoS2 Nanosheet-Based

Nanocomposite toward High-Performance Ammonia Detection, *ACS Appl. Mater. Interfaces*, 2017, **9**(7), 6462–6471.
27 D. Zhang, *et al.*, Metal-organic frameworks-derived hollow zinc oxide/cobalt oxide nanoheterostructure for highly sensitive acetone sensing, *Sens. Actuators, B*, 2019, **283**, 42–51.
28 D. Zhang, *et al.*, Fabrication of platinum-loaded cobalt oxide/molybdenum disulfide nanocomposite toward methane gas sensing at low temperature, *Sens. Actuators, B*, 2017, **252**, 624–632.
29 K. Białas, *et al.*, Electrochemical sensors based on metal nanoparticles with biocatalytic activity, *Microchim. Acta*, 2022, **189**(4), 172.
30 X. Dai, *et al.*, Determination of serum uric acid using high-performance liquid chromatography (HPLC)/isotope dilution mass spectrometry (ID-MS) as a candidate reference method, *J. Chromatogr. B*, 2007, **857**(2), 287–295.
31 R. Singh and J. Singh, Recent advances in nanostructured cobalt oxide (Co3O4): Addressing methods and design strategies, challenges, and future directions for non-enzymatic sensor applications, *Sens. Actuators, A*, 2025, **387**, 116404.
32 A. Nandagudi, *et al.*, Hydrothermal synthesis of transition metal oxides, transition metal oxide/carbonaceous material nanocomposites for supercapacitor applications, *Mater. Today Sustain.*, 2022, **19**, 100214.
33 P. G. Kannan, *et al.*, Maduraiveeran Metal Oxides Nanomaterials and Nanocomposite-Based Electrochemical Sensors for Healthcare Applications, *Biosensors*, 2023, **13**(5), 542.
34 K. O. Abdulwahab, M. M. Khan and J. R. Jennings, Ferrites and ferrite-based composites for energy conversion and storage applications, *Crit. Rev. Solid State Mater. Sci.*, 2024, **49**(5), 807–855.
35 P. Ahuja, *et al.*, Transition Metal Oxides and Their Composites for Photocatalytic Dye Degradation, *J. Compos. Sci.*, 2021, **5**(3), 82.
36 C. Mutalik, *et al.*, Antibacterial Pathways in Transition Metal-Based Nanocomposites: A Mechanistic Overview, *Int. J. Nanomed.*, 2022, **17**, 6821–6842.
37 S. Yadav, N. Rani and K. Saini, A review on transition metal oxides based nanocomposites, their synthesis techniques, different morphologies and potential applications, *IOP Conf. Ser.: Mater. Sci. Eng.*, 2022, **1225**(1), 012004.
38 S. Naeem, *et al.*, A Review of Cobalt-Based Metal Hydroxide Electrode for Applications in Supercapacitors, *Adv. Mater. Sci. Eng.*, 2023, **2023**(1), 1133559.
39 R. S. Kate, S. A. Khalate and R. J. Deokate, Overview of nanostructured metal oxides and pure nickel oxide (NiO) electrodes for supercapacitors: A review, *J. Alloys Compd.*, 2018, **734**, 89–111.
40 S. J. Mammadyarova, Synthesis and characterization of cobalt oxide nanostructures a brief review, *Azerbaijan Chem. J.*, 2021, (2), 80–93.
41 S. Mehmood, Z. Yiqiang and S. Sagadevan, Cobalt oxide-based nanomaterial for electrochemical sensor applications: A mini review, *Malaysian NANO-An Int. J.*, 2021, **1**(1), 47–63.
42 S. B. Mayegowda, *et al.*, 27 – Sustainability and green nanomaterials on nanotechnology-based sensors, in *Nanotechnology-based Sensors for Detection of Environmental Pollution*, F. M. Policarpo Tonelli, et al., Elsevier, 2024, pp. 553–572.
43 K. Malik, *et al.*, *A Mechanistic Overview on Green Assisted Formulation of Nanocomposites and Their Multifunctional Role in Biomedical Applications*. 2025.
44 S. Mallek-Ayadi, *et al.*, Bioactive compounds from Cucumis melo L. fruits as potential nutraceutical food ingredients and juice processing using membrane technology, *Food Sci. Nutr.*, 2022, **10**(9), 2922–2934.
45 V. V. Poborchii, *et al.*, Single crystal polarization-orientation Raman spectroscopy of zeolite LTA with confined S3- anions - High dielectric constant nanoporous material, *Mater. Chem. Phys.*, 2024, **316**, 129103.
46 S. Taheri, *et al.*, Removal notice to Sustainable concrete design using waste latex paint, *Sustain. Mater. Technol.*, 2024, e01147.
47 N. Alizadeh, *et al.*, CuO/WO3 nanoparticles decorated graphene oxide nanosheets with enhanced peroxidase-like activity for electrochemical cancer cell detection and targeted therapeutics, *Mater. Sci. Eng.,C*, 2019, **99**, 1374–1383.
48 S. Vijayakumar, S. Nagamuthu and G. Muralidharan, Supercapacitor Studies on NiO Nanoflakes Synthesized Through a Microwave Route, *ACS Appl. Mater. Interfaces*, 2013, **5**(6), 2188–2196.
49 S.-I. Kim, *et al.*, Facile Route to an Efficient NiO Supercapacitor with a Three-Dimensional Nanonetwork Morphology, *ACS Appl. Mater. Interfaces*, 2013, **5**(5), 1596–1603.
50 X. Su, *et al.*, A novel platform for enhanced biosensing based on the synergy effects of electrospun polymer nanofibers and graphene oxides, *Analyst*, 2013, **138**(5), 1459–1466.
51 A. S. Chang, *et al.*, Silky Co_3O_4 nanostructures for the selective and sensitive enzyme free sensing of uric acid, *RSC Adv.*, 2021, **11**(9), 5156–5162.
52 A. R. West, *Solid State Chemistry and its Applications*, John Wiley & Sons, 2022.
53 Y. Gao, *et al.*, Synthesis of Co3O4-NiO nano-needles for amperometric sensing of glucose, *J. Electroanal. Chem.*, 2019, **838**, 41–47.
54 F. T. Munna, *et al.*, Diluted chemical bath deposition of CdZnS as prospective buffer layer in CIGS solar cell, *Ceram. Int.*, 2021, **47**(8), 11003–11009.
55 H. Li, *et al.*, Role of the in situ formed LiAl(NH)2 and LiNH2 in significantly improving the hydrogen storage properties of the Mg(NH2)2-2LiH systems with Li3AlH6 addition, *J. Alloys Compd.*, 2024, **1002**, 175260.
56 P. Lamba, *et al.*, Bioinspired synthesis of nickel oxide nanoparticles as electrode material for supercapacitor applications, *Ionics*, 2021, **27**(12), 5263–5276.
57 Y. Cao, P. Hu and D. Jia, Solvothermal synthesis, growth mechanism, and photoluminescence property of sub-

micrometer PbS anisotropic structures, *Nanoscale Res. Lett.*, 2012, **7**(1), 668.
58 H.-J. Choi, *et al.*, Graphene for energy conversion and storage in fuel cells and supercapacitors, *Nano Energy*, 2012, **1**(4), 534–551.
59 B. Chandran, *et al.*, Cerium Zirconium Oxide-Decorated Reduced Graphene Oxide Nanocomposite for Low Potential Voltammetric Detection of N-Hydroxysuccinimide, *ACS Appl. Nano Mater.*, 2024, **7**(7), 6839–6850.
60 C. Bhuvaneswari, *et al.*, Voltammetric nano-molar range quantification of agrochemical pesticide using needle-like strontium pyrophosphate embedded on sulfur doped graphitic carbon nitride electrocatalyst, *Food Chem.*, 2024, **437**, 137874.
61 S. H. Han, *et al.*, Electrochemical detection of uric acid in undiluted human saliva using uricase paper integrated electrodes, *Sci. Rep.*, 2022, **12**(1), 12033.
62 H. L. S. Santos, *et al.*, NiMo–NiCu Inexpensive Composite with High Activity for Hydrogen Evolution Reaction, *ACS Appl. Mater. Interfaces*, 2020, **12**(15), 17492–17501.
63 V. Selvanathan, *et al.*, Resorcinol-Formaldehyde (RF) as a Novel Plasticizer for Starch-Based Solid Biopolymer Electrolyte, *Polymers*, 2020, **12**(9), 2170.
64 M. Akbayrak and A. M. Önal, Metal oxides supported cobalt nanoparticles: Active electrocatalysts for oxygen evolution reaction, *Electrochim. Acta*, 2021, **393**, 139053.
65 Z. Han, *et al.*, Dual regulation of anode corrosion and cathode oxygen evolution in alkaline sodium-ion batteries by hydrated eutectic electrolyte engineering, *Chem. Eng. J.*, 2026, **531**, 174384.
66 P. Uful, *et al.*, Advanced flexible supercapacitors:vertical 2D MoS2 and WS2 nanowalls on graphenated carbon nanotube cotton, *Nanoscale*, 2025, **17**, 6704–6717.
67 F. Mazzara, *et al.*, Electrochemical detection of uric acid and ascorbic acid using r-GO/NPs based sensors, *Electrochim. Acta*, 2021, **388**, 138652.
68 V. Nagal, *et al.*, A non-enzymatic electrochemical sensor composed of nano-berry shaped cobalt oxide nanostructures on a glassy carbon electrode for uric acid detection, *New J. Chem.*, 2022, **46**(25), 12333–12341.
69 A. G. Solangi, *et al.*, Green-Mediated Synthesis of NiCo2O4 Nanostructures Using Radish White Peel Extract for the Sensitive and Selective Enzyme-Free Detection of Uric Acid, *Biosensors*, 2023, **13**, 780.
70 V. Nagal, *et al.*, Highly Sensitive Electrochemical Non-Enzymatic Uric Acid Sensor Based on Cobalt Oxide Puffy Balls-like Nanostructure, *Biosensors*, 2023, **13**(3), 375.
71 Y. Chen, *et al.*, Nonenzymatic Sweat Wearable Uric Acid Sensor Based on N-Doped Reduced Graphene Oxide/Au Dual Aerogels, *Anal. Chem.*, 2023, **95**(7), 3864–3872.
72 C. Wang, *et al.*, A wearable flexible electrochemical biosensor with CuNi-MOF@rGO modification for simultaneous detection of uric acid and dopamine in sweat, *Anal. Chim. Acta*, 2024, **1299**, 342441.
73 Y. Zhao, *et al.*, ZnS and Reduced Graphene Oxide Nanocomposite-Based Non-Enzymatic Biosensor for the Photoelectrochemical Detection of Uric Acid, *Biosensors*, 2024, **14**, DOI: 10.3390/bios14100488.